Shape stability and flow behaviour of a phase change material based slurry in coupled fluid-thermo-electrical fields for electronic device cooling

Li, Qi; Mura, Ernesto; Li, Chuan; Pignataro, Marco; Qiao, Geng; Fischer, Ludger; Ding, Yulong

Document Version
Peer reviewed version

[Link to publication on Research at Birmingham portal](#)

Journal Pre-proofs

Shape stability and thermodynamic study of phase change material slurry under fluid-thermo-electric coupled fields for electronic device cooling

Qi Li, Ernesto Mura, Chuan Li, Marco Pignataro, Geng Qiao, Ludger Fischer, Yulong Ding

Please cite this article as: Q. Li, E. Mura, C. Li, M. Pignataro, G. Qiao, L. Fischer, Y. Ding, Shape stability and thermodynamic study of phase change material slurry under fluid-thermo-electric coupled fields for electronic device cooling, *Applied Thermal Engineering* (2020), doi: https://doi.org/10.1016/j.applthermaleng.2020.115117

Shape stability and thermodynamic study of phase change material slurry under fluid-thermo-electric coupled fields for electronic device cooling

Qi Li[a], Ernesto Mura[b], Chuan Li[a*], Marco Pignataro[a], Geng Qiao[b], Ludger Fischer[c], Yulong Ding[a,*]

[a] Birmingham Centre for Energy Storage (BCES) & School of Chemical Engineering, University of Birmingham, United Kingdom B15 2TT, UK

[b] Global Energy Interconnection Research Institute Europe GmbH, 10623 Berlin, Germany

[c] Lucerne University of Applied Sciences and Arts, Horw 6048, Switzerland

*Corresponding authors. Email address: c.li.4@bham.ac.uk (C. Li); Y.Ding@bham.ac.uk (Y. Ding)

Abstract

The suitable melting range and low electrical conductivity of fatty acid-based Phase Change Material (PCM) slurry make it desirable in High–Voltage Direct Current (HVDC) electronic device cooling, but the shape instability hazard introduced by external electrical field may alter the slurry effective properties and affect the heat transfer performance. In this work, the shape stability and thermodynamic performance of a fatty acid droplet under fluid-thermo-electric coupled field are numerically investigated. The effects of droplet size, fluid velocity and temperature, and electric field on shape and energy evolution of the droplet are evaluated. The results show the droplet size is the major influencing factor to shape stability, and 1 μm droplet presents 8 times higher deformation ratio and 5 times larger internal pressure difference than the 7 μm ones. The growth of slurry velocity only slightly increases the particle interior pressure, about 25.77% when velocity increasing from 0.22 m/s to 1.1 m/s for a given droplet. The electric stress across surface tends to squeeze the droplet into prolate shape, which offsets the shape deformation by shear stress and stabilizes PCM slurry system. The presence of electrical field slows down the energy evolution and reduces the pressure difference inside the droplet.

Keywords: Fatty acid; Phase changes material slurry; Shape stability; Fluid-thermo-electric Multiphysics field; Energy evolution; Thermal-fluidic performance

1. Introduction

Along with the rapid growth in power ratings and persistent miniaturization of HVDC electronic devices, heat fluxes projecting to megawatt range are now well beyond the domain of conventional thermal management techniques [1, 2]. Power dissipation of 9.72 kW is detected in high power HVDC converter system, which occupies up to 30% of the whole loss power [3, 4]. The conventional cooling technologies, such as air cooling or water cooling, are normally suitable for lower power electronic devices below a rough range of 1.5 W dissipation [5]. For high power electronic devices, thermal enhancement can be realized by dispersing and transporting PCM in thermal-active fluid by use of immiscible fluids (PCM slurry). In the case of electronic cooling, the PCM slurry components are best to be insulting material to ensure long-term running in high voltage environment.

As an organic dielectric media, fatty acid is widely used due to the low chemical inertness, flexible application and low electrical conductivity [6, 7]. It can be easily produced from common vegetable and animal oils and thus provide an assurance of continuous supply despite the shortage of fuel sources [8, 9]. The fatty acid normally works in the ambient-to-moderate temperature range [10] (20 - 100 °C), which is suitable for most electronic devices cooling [11] (around 60 °C). The electrical conductivity of the fatty acid can reach as low as 10^{-10} S/m [12], which is lower than the deionized water (5.5×10^{-8} S/m). Hasan et al. [11] proved the milk fat (riches with fatty acid) had the potential for electronic cooling. Kahwaji et al. [13] compared three types of fatty acids with melting range of $30 - 70°C$ and enthalpy changes larger than 145 J/g. The acids are proved to perform thermally stable over 3000 times in a steady state.

One barrier in application of PCM emulsion is the difficulty in maintaining stability of the PCM droplets during the phase change transition [14]. In theory, the stabilization of a droplet is determined by the size, interfacial tension, emulsifier thickness and emulsifier structure etc. [15]. It must be noted that external physical field, such as electric, thermal or fluid field, is another important factor influencing slurry stability in practical condition. In the presence of electric field, a steady drop suspended in insulting viscous liquid may experience complex behaviours (e.g. deformation, electroporation and burst) due to electrical polarization stress and thus performing different thermodynamic feature. A numerical study by Dong and Sau [16] found an insulting droplet may break into a number of a satellite drops when exposed to electrical field. Ouriemi and Vlahovska [17] and Mikkelsen et al. [18] found the electrical field strongly influents the surface-absorbed particles/surfactant distribution on droplet surface under electrical field. The deformed shape may alter the effective thermal conductivity and viscosity, leading to a changed pressure drop and heat transfer coefficient [19, 20]. For example, the cooling performance of platelets particle could be 53% worse than the base fluid, because the high viscosity degrades the effect of higher thermal conductivity

[20]. Additionally, the electrokinetics and thermal transport of electrolyte has been studied by Das et al. [21-23] in a wide range, showing that the overall electric double layer (EDL) electrostatic potential distribution results in a significant reduction of the effective EDL thickness, thus be of overwhelming significance in nanofluidic transport. However, the cross-stream migration driven by electric field [24] or temperature gradient [25] may accelerates or slows down the PCM energy charging rate but still unclarified in the field of energy storage.

To understand the thermodynamic feature of slurry/capsules system, a single PCM droplet / particle is normally employed to explore the energy storage and stability performance. Yu et al. [26] numerically studied the effect of density variation on energy storage capacity of a 1 mm PCM capsule during phase change transition, and found the energy charging rate of PCM is notably different from those without considering property variations. Similarly, a numerical study from Zhao et al. [27] found that the melting process is longer for large particle in thermocline operation, and both spatial and temporal temperature changes are important for heat transfer performance. During the phase change process with heat transmittance for the PCM droplet, expansibility will appear coming from thermophysical property variation. A noteworthy fact is that these work only considered the ambient pressure of shell surface, while the significant importance of the shear stress and fluid pressure gradient was ignored. When emulsion exposed to high shear rates, it may break into smaller sizes, or burst the emulsifier shields to form a bigger droplet and ultimately results in complete breakdown of emulsions [24].

Motived by this, a comprehensive study considering the shear stress from fluid field, thermophysical expansion from thermal field, and electrical polarization from electrical field on stability of PCM slurry is needed. This paper presents a first attempt to numerically analyse the thermodynamic performance of a fatty acid droplet in a fluid-thermo-electric coupled field. In what follows, the fatty-acid PCM slurry developed for HVDC cooling is characterized under different temperatures. The mathematical models are then demonstrated and implemented in CFD software FLUENT 18.2 via User Defined Function (UDF), using temperature-dependence properties. To include the influence of mobile electric charges, the model assumes a constant total electric charge over the droplet interface. The model is first validated with literature values, followed with the comprehensive discussion of shape stability and energy evolution under different droplet sizes, velocities, water temperatures and electrical field. Present work enriches theory guidance of shape stability and energy storage performance for PCM slurry application in electronic device cooling.

2 Mathematical models

Fig. 1 shows the schematic of the computational domain within two parallel plates. In a typical water cooling heat sink for HDVC converter transmission systems, fluid channel size (~ cm) is beyond the range of micro-size PCM droplets, meaning a negligible wall effect on

droplet deformation. As a result of this, a two-dimension domain of $H_{tot} = 40D$ width and $L_{tot} = 160D$ length is employed to reduce calculation cost, yet long enough for droplet melting and stabilization. The inlet boundary is a fully developed parabolic Poiseuille flow (average velocity of U) with constant inflow temperature T=329.15 K, which is chosen just above the PCM liquidus point. The initial droplet temperature is 318.16 K as it very close to the PCM solidius temperature. The inlet velocity varies between 0.22 m/s to 1.1 m/s, which is the typical operational conditions in water cooling devices of HVDC converter (provided by Global Energy Interconnection Research Institute Europe GmbH/GEIRI, Germany). The Newtonian PCM droplet is initially placed 10D away from inlet of the fluid centreline, and moves freely in a water environment. A constant water temperature equal to the inflow temperature is kept by setting thermal isolation parallel plates. An equal value of positive and negative electric potential is applied at the upper and lower plate, respectively, to generate a uniform electric field pointing toward the lower plate. Atmospheric pressure (101,325 Pa) is used as the exit boundary. No-slip condition is applied to all wall boundaries.
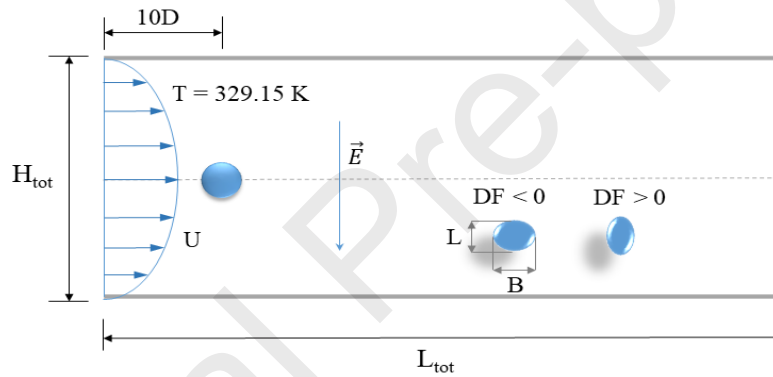
Fig. 1. Schematic of the computational domain within two parallel plates. The initial droplet diameter is D. Two shape deformation conditions are given for DF < 0 and DF > 0.

The droplet is composed of a 16 wt.% fatty acid-based PCM and a 4 wt.% Steareth emulsifier, suspended in a 80 wt.% deionized water environment. Thermal properties of droplet material are measured and provided by GEIER (Germany) company and Lucerne University of Applied Sciences and Arts. The droplet density decreases from 923.88 kg/m³ at 298.15 K to 862.82 kg/m³ at 329.15 K, following a linear decreasing function. The thermal conductivity of the droplet decreases linearly from 0.243 W/(m·K) at 298.15 K to 0.225 W/(m·K) at 329.15 K. The solidius (melting) and liquidus temperature of the droplet is 319.16 K and 327.49 K, respectively. Latent heat during the melting process is 183010 J/kg. The viscosity of the droplet decreases linearly from 122.15 mPas at 319.16 K to 90.27 mPas at 329.15 K. The electrical conductivities of the droplet and water is 10e-11 S/m and 5.5e-06 S/m, respectively, and the permittivities is 1.8e-11 F/m and 7.08e-10 F/m, respectively. The surface tension coefficient between the droplet and water follows a decreasing trend with

increasing temperature, $\sigma = 0.079 - 0.00002T$. To accurately describe the variation of C_p with temperature, the piecewise-linear method is implemented directly in FLUENT, as given in Fig. 2. Consider the small temperature shift of water, the density, thermal conductivity, specific heat and dynamic viscosity is chosen to be constant value of 998.2 kg/m³, 0.6 W/(m·K), 4182 J/(kg·K) and 0.001003 kg/(m·s), respectively.
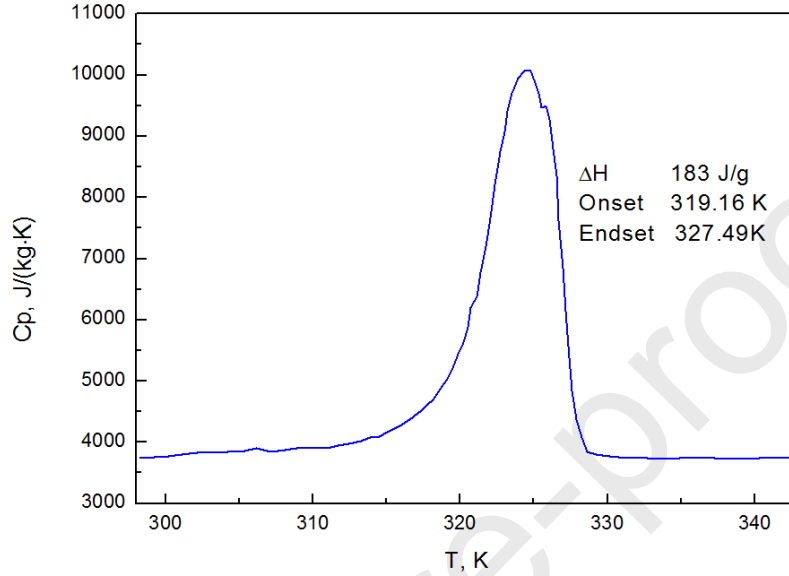
Fig. 2. Specific heat capacity of droplet material over a temperature of 298 K to 343 K.

2.1. Fluid and energy governing equations

The two-phase hydrodynamic flow coupled melting process with uniform direct DC electric field is solved in FLUENT using the Volume of Fluid (VOF) model, which can accurately capture the free interface between the PCM droplet and water. The Continuum Surface Force (CSF) method treats two phases as a single fluid with space-dependent properties and replaces the interface boundary with an additional force [28]. To take into account the surface tension and electric stress, the Navier-Stokes equations needs to be modified by adding body forces in the momentum equation:

Continuity:

$$\nabla \cdot \vec{u} = 0 \tag{1}$$

Momentum:

$$\frac{\partial(\rho\vec{u})}{\partial t} + \nabla \cdot (\rho\vec{u}\vec{u}) = -\nabla p + \nabla \cdot \left[\mu(\nabla\vec{u} + (\nabla\vec{u})^{\mathrm{T}})\right] + \vec{F_s} + \vec{F_E} \tag{2}$$

Thermal energy:

$$\frac{\partial(\rho c_p T)}{\partial t} + \nabla \cdot \left(\rho c_p \vec{u} T \right) = \nabla \cdot (k \nabla T) + \Phi \tag{3}$$

where $\vec{u}$, ρ, p, μ, T, c_p and k are the velocity, density, pressure, dynamic viscosity, thermodynamic temperature, specific heat and thermal conductivity of the total fluid, respectively. $\overrightarrow{F_s}$ and $\overrightarrow{F_E}$ represent the interfacial tension force and electric body force acting at the droplet interface, respectively. Φ is a dissipate term which can be neglected due to a small Eckert number [29]. The interfacial tension acting normal to the interface is given as:

$$\overrightarrow{F_s} = \sigma \kappa \vec{n} \delta_\Gamma \tag{4}$$

where κ is the local interface curvature; $\vec{n}$ is the unit normal to the interface, and δ_Γ is the Dirac delta function used to localize the force explicitly at the interface [30], which should satisfy

$$\int_{-\infty}^{\infty} \delta_T dz = 1 \tag{5}$$

where z represents the spatial location normal to the interface. It can recover the stress jump condition properly in the sharp-interface limit [28]. To capture the free interface between the droplet and surrounding fluid, an additional transport equation for volume fraction C is solved and given as:

$$\frac{\partial C}{\partial t} + \nabla(\vec{u}C) = 0 \tag{6}$$

Here C is 0 and 1 when cell is full of dispersed and main phase, respectively, and $0 < C < 1$ when the interface of two phases exists in the cell. With the VOF-variable the fluid density and viscosity at interface can be defined as:

$$\rho(x,t) = \rho_d + (\rho_c - \rho_d) C(x,t) \tag{7}$$

$$\mu(x,t) = \mu_d + (\mu_c - \mu_d) C(x,t) \tag{8}$$

The specific heat and thermal conductivity across the interface are calculated in a similar way with the VOF-variable. The stored energy balance within the droplet is calculated as the sum of latent heat and sensible energy:

$$E(\beta) = \Delta H_L + \Delta H_S = \int_0^\beta \rho(\theta)V(\theta)L_m d\vartheta + \int_0^{V_{eq}} \int_{T(\beta=0)}^{T(\beta)} \rho(T)c_p(T)dTdV \tag{9}$$

Where L_m is the melting latent heat, β is the liquidus fraction inside droplet depending on local temperature. In particular β is 0 when the temperature in computational cells is below solidus point ($T < T_S$), 1 when above liquidus temperature ($T > T_L$), and equal to $(T - T_S)/(T_l - T_S)$ for $T_S < T < T_L$. The improved Stefan number considering the thermos-

physical variation during melting is defined as the ratio of sensible to latent heat $Ste = \Delta H_S / \Delta H_L$. The temporal mass-weighted average of the droplet temperature is given by:

$$T_{avg} = \frac{\sum_{i=1}^{n} T_i \rho_i |\overrightarrow{u_i A_i}|}{\sum_{i=1}^{n} \rho_i |\overrightarrow{u_i A_i}|} \tag{10}$$

where T_i is the fluid temperature at the location of i inside droplet. The temporal drop surface average temperature, T_s, is calculated by averaging the temperature of the droplet surface at iso-surface of $C = 0.5$. The effective heat transfer coefficient during melting can thereby be obtained:

$$h_{eff} = \frac{E(\beta_i)}{\Delta t_i A_i (T_w - T_{s,i})} \tag{11}$$

Where A_i is the droplet surface area at time i, Δt_i is the melting time, $T_{s,i}$ is the surface temperature at i moment.

2.2. Electrical field

The electric stress in Eq. (2) can be calculated by taking the divergence of a Maxwell stress tenser (τ^M):

$$\overrightarrow{F_E} = \nabla \cdot \tau^M = \underbrace{-\frac{1}{2}\overrightarrow{E} \cdot \overrightarrow{E} \nabla \varepsilon}_{Polarization\ electric\ stress} + \underbrace{q^V \overrightarrow{E}}_{\substack{charge - field\ interaction \\ electric\ stress}} + \underbrace{\nabla \left(\frac{1}{2}\overrightarrow{E} \cdot \overrightarrow{E} \frac{\partial \varepsilon}{\partial \rho} \rho \right)}_{electrorestriction\ force\ density}$$

$$\tag{12}$$

where q^V is the volume charge density near the interface. The first term is the polarization electric stress acting on along the normal direction of droplet interface, and the second term charge-field interaction electric stress acts along the direction of electric field. The electrorestriction force density is neglected due to an incompressible fluid. The Gauss law is used to calculate q^V in terms of electric displacement:

$$\nabla \cdot \overrightarrow{D} = \nabla \cdot \left(\varepsilon \overrightarrow{E} \right) = q^V \tag{13}$$

Thus the charge conservation can be calculated as follows:

$$\frac{Dq^V}{Dt} = \frac{\partial q^V}{\partial t} + \overrightarrow{U} \cdot \nabla q^V = - \nabla \cdot \left(\sigma \overrightarrow{E} \right) \tag{14}$$

where D()/Dt is the material derivative. Combining the above two equations, we obtain equations for free charges:

$$\left[\frac{\partial}{\partial t} + \overrightarrow{U} \cdot \nabla \right] q^V = \frac{Dq^V}{Dt} = - \frac{\sigma}{\varepsilon} q^V = 0 \tag{15}$$

$$q^v = q_0^v e^{-\sigma/\varepsilon t} \tag{16}$$

where q_0^v is the initial volume free charge density decreasing with t^E. In electrodynamics, two time scales are proposed to identify the free charge density: the electric relaxation time ($t^E = \varepsilon/\sigma$) and viscous time scale of fluid motion ($t^v = \rho L^2/\mu$), where L is the fluid characteristic length scale [31, 32]. The leaky condition, assuming the free charges accumulate almost instantaneously and has no effects of fluid motion as $t^E \ll t^v$, is used in the current study. This simplified model is normally validated only at low charge density with limited droplet deformation ($Ca_E < 0.2$, $|D| < 0.05$). It greatly simplified charge process because the charge resident process is neglected [33]. Based on above assumptions, the charge conservation equation can be simplified as:

$$\nabla \cdot (\sigma \vec{E}) = 0 \tag{17}$$

where the electric field ($\vec{E}$) is defined as the gradient of electric potential, $\vec{E} = -\nabla\phi$. Hence the charge conservation equation can be expressed as:

$$\nabla \cdot (\varepsilon\nabla\phi) = 0 \tag{18}$$

Therefore the direction of polarization electric stress in Eq. (12) is pointing from high to low permittivity due to the gradient of electrical permittivity, and the charge-field interaction electric stress only exists across the droplet interface due to the electrical permittivity gradient. Taylor et al. [34] proposed a droplet deformation correlation based on electric Capillary number ($Ca_E = E^2\varepsilon_c R/\sigma$), ratio of permittivity ($P = \varepsilon_d/\varepsilon_c$), conductivity ($S = \eta_d/\eta_c$) and viscosity under constant electrical field as given by:

$$DF = \frac{L-B}{L+B} = \frac{9Ca_E}{16(S+1)^2}\left[S^2 + 1 - 2P + 3(S-P)\frac{2+3\lambda}{5(1+\lambda)}\right] \tag{19}$$

Where L and B are respectively the length of the parallel and perpendicular axis of deformed droplets with respect to the electric field, ε and η are the permittivity and conductivity of fluid, respectively.

Non-dimensional parameters involved in solving the thermal features of droplet loading fluid are Fourier number, Prandtl number, Reynolds number and Nusselt number. The Fourier number is the dimensionless time for a temperature change to occur, defined as $Fo = t\alpha_c/R_0^2$, where t is the characteristic time, $\alpha_c = k_c/(c_{p,c}\cdot\rho_c)$ is the thermal diffusivity, R_0 is the initial droplet radius, k_c, $C_{p,c}$ and ρ_c are the thermal conductivity, specific heat capacity and density of continuous phase, respectively. Prandtl number of local phase is defined as $Pr = c_p\mu/k$, representing the ratio of momentum diffusivity to thermal diffusivity. Reynolds number represents the ratio of inertial force to viscous force as $Re = \rho_c UD/\mu_c$. Nusselt number is the

ratio of convective to conductive heat transfer, given by $Nu = h_{eff}D/k$, where h_{eff} is the effective heat transfer coefficient.

The major assumptions in simplifying the governing equation and boundary conditions are as follows: 1) Gravitational and inertial forces are neglected due to the small Bo number (Bo <<1) and low Reynolds number, respectively, 2) Drop-drop interaction is not considered due to reasonable surfactant coverage and low Capillary number, 3) The interfacial tension is linearly dependent on temperature only, whereas the effect of electricity is ignored, 4) The free charges accumulate almost instantaneously and have no effects of fluid motion, 5) The total electric charge is a constant value during simulation process, 6) Both fluids are assumed to be incompressible, immiscible and Newtonian fluid.

The first order upwind and Green-Gauss node based on gradient calculation schemes are used for time marching of momentum/continuity equations and the pressure gradient calculations [35, 36], respectively. The time step is controlled by specified maximum value for the Courant number, $Co = \Delta t/(\Delta x/U)$, where Δt, Δx and U are the time step, grid size and fluid velocity, respectively. A low Co of 0.1 using very small time step (1e-08) is adopted in the current work due to very fine elements close to the interface. The steady residuals were found to be sufficiently low, O (10^{-9}) for continuity, O (10^{-8}) for energy and O (10^{-14}) for electricity.

3. Results and discussion

3.1. Model validation

To validate the proposed model, simulations are first conducted and compared with previous work in Fig. 3, using a fluid system of 200F silicone oil droplet in oxidized castor-oil medium. Various grid combination are tested inside the droplet and surrounding domain, from D/h = 5 (D and h is the droplet diameter and grid size, respectively) to D/h = 64. It is found that D/h = 32 near the droplet zone gives an accurate prediction with the smallest mesh number (discussion given below). The grid size gradually increases by 25% until reaching D/h =10 near the parallel plates. The mesh contains nearly 5 million cells in the entire domain, proven to sufficiently capture the interface phenomenon and resolve the flow field around the droplet [37, 38].

Fig. 3 shows the model validation of droplet deformation rate under various electrical field intensities. The results from current proposed model are compared with theory (Eq. (19)) from Taylor et al. [34], experimental work from Torza et al. [39] and simulation from Wang et al. [31]. Using the mesh size of D/h=16, 32 and 64, present work yields averaged deviation of 12.71%, 4.40 % and 3.85% compared to experimental results, respectively. To further examine the grid quality, the interior velocity field inside a steady droplet is compared with Wang et al. [31] under permittivity ratio P = 0.3 and conductivity ratio S = 0.265, using D/h =

32 grid in Fig. 4. The four steady circulations along the interface are generated due to the shear stress at the interface generated by accumulated charge. The results obtained in this study show a satisfactory agreement with the literature, indicating that both the grid quality and proposed model is sufficiently accurate.
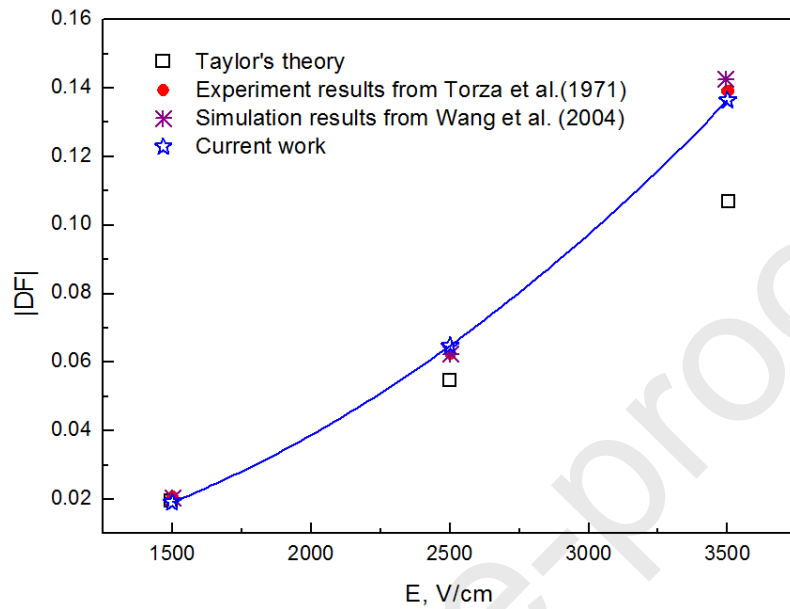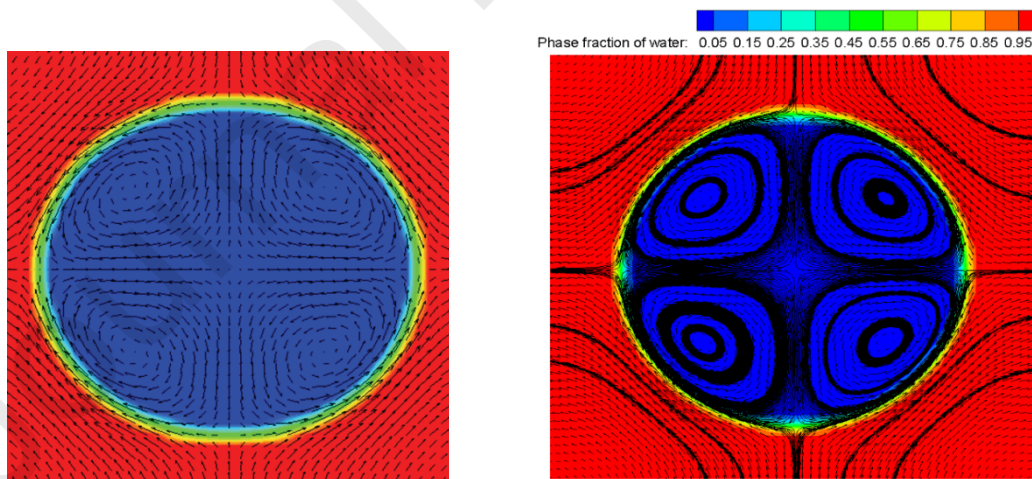

Fig. 3. Model validation of droplet deformation rate under electrical field strength variations. Compared with theory from Taylor et al. [34], experimental results from Torza et al. [39] and simulation work from Wang et al. [31].

| i) DF = -0.065 | ii) DF = -0.0627 |

(a) P = 0.3

10

i) DF = -0.18   ii) DF = -0.18
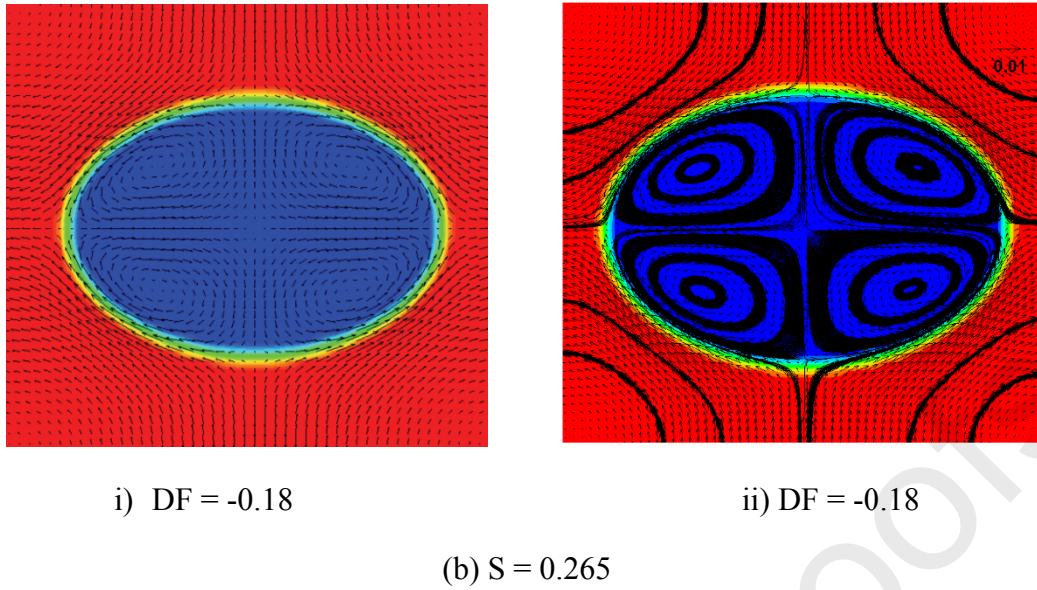
(b) S = 0.265

Fig. 4. Model validation on droplet deformation, i) and ii) array refers to results from Wang et al. [31] and current work, respectively. Case (a) and (b) denotes to permittivity ratio and conductivity ratio of P = 0.3 and S = 0.265, respectively.

3.2. Effect of droplet size

An example of instantaneous contours of the melting (liquid) fraction, temperature, density and pressure field inside a 3μm droplet is depicted over the dimensionless time, Fo, in Fig. 5. The melting fraction (top) and temperature (bottom) contours are given in (i) array; whereas density (top) and pressure (bottom) contours are shown in (ii) array. The PCM droplet moves from left to right in an average water velocity of 0.66 m/s. The natural convection caused by the density difference of solid and liquid region inside such small size scale can be ignored. Upon quick melting of PCM, a liquid film surrounding the droplet internal surface forms due to diffusion-controlled melting. The temperature across the droplet interface is non-uniformly distributed when exposed to surrounding fluid, as shown in the bottom part of (i) array of Fig. 5. Temperature gradients tangential to the liquid surface produce surface tension gradient and induce local tangential flows, especially the front facing part (discussed in the following part). As a result, heat transfer near the front facing interface is enhanced, leading to a less melted and lower temperature zone located at the back of droplet. A similar density pattern is found in the top view of Fig. 5(a-ii) and (b-ii), whereas the bottom views show high pressures existing near the front melting zone, due to the impinging effect of incoming external fluid. With the progress of droplet movement, the distribution of the above melting features becomes uniform under the combination effect of diffusion-control melting and convection. When the droplet is fully melted (Fo = 4), a large pressure gradient is found at droplet edge.

11
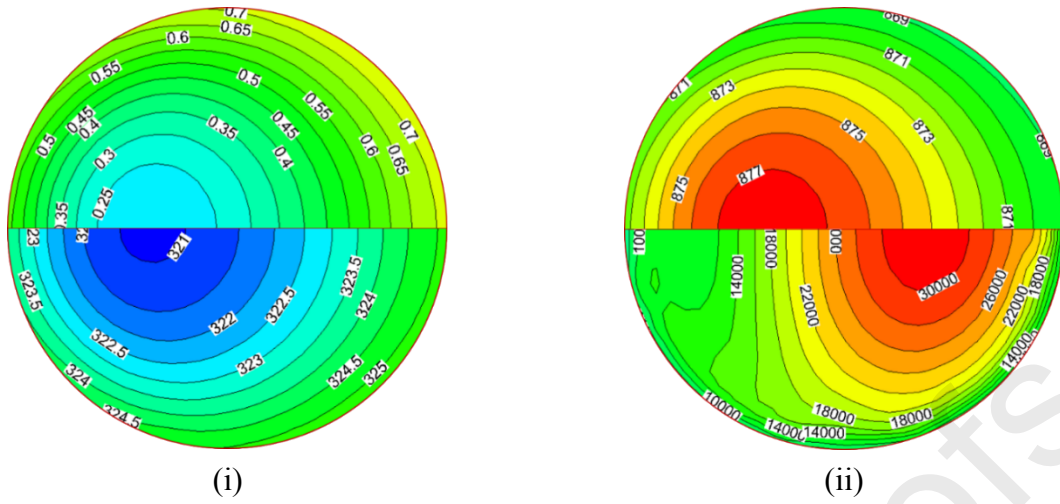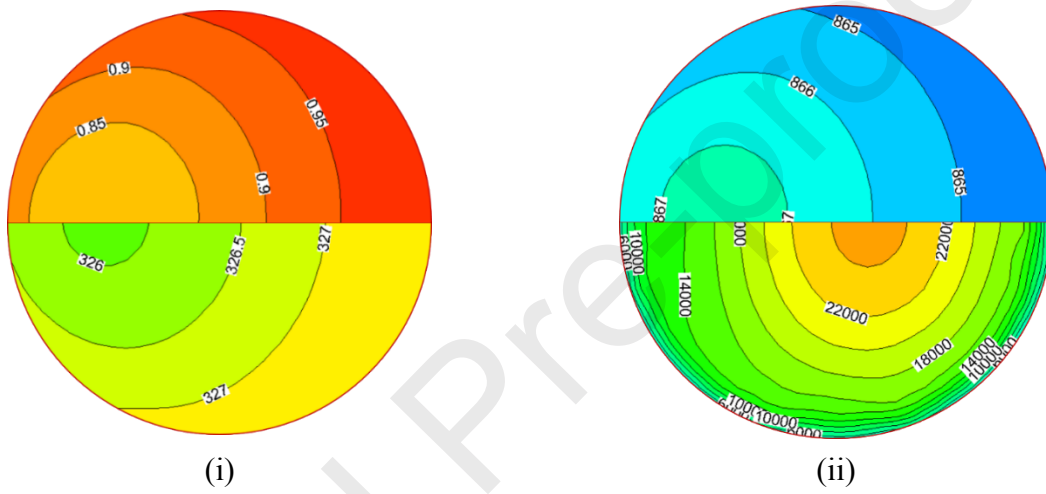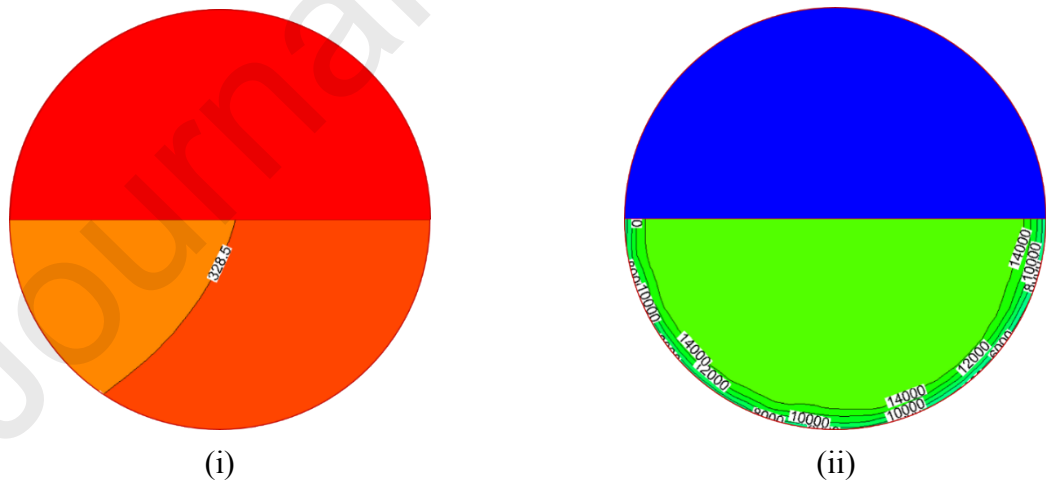
(a) Fo = 0.012

(b) Fo = 0.31

(c) Fo = 4.00

Fig. 5. The evolution of the melting fraction (top) and temperature (bottom) in (i) array contours, and density (top) and pressure (bottom) in (ii) array contours, for ID = 3 μm and U = 0.66 m/s over different Fo time. Flow direction is from left to right.

12

Fig. 6 illustrates the effect of droplet diameter on deformation rate under the same inlet velocity. The deformation rate is given as $DF = (L - B)/(L + B)$, where L and B are respectively the longitudinal (y direction) and transverse (x direction) diameters of the droplet. An example of 3 μm droplet shape deformation evolution is given in the inset graph. The dimensionless area, calculated as the ratio of transient droplet area A with initial area A_0, is depicted over Fo time. Droplet area is found to increase with the progress of melting as a result of a force balance between pressure force and drag force, and reaches a steady state after Fo = 0.4. Another noteworthy reason of area increment is that droplet volume is slightly expanded due to the density decrease in the melting process. Meanwhile, the value fluctuates within a small local range throughout the whole process, due to the oscillation of the small moving droplet [40] and variant thermos-physical properties. Similar phenomena can also be found in a bubble deformation [29, 41]. For the purpose of theory comparison, such as Eq. (19), the deformation rate (DF) at the steady state is used, which gives both deformation extent and direction (oblate for DF <0 and probate for DF >0). As shown in Fig. 6, the oscillation is taken into account by form of deviations, which reaches highest value of 33.8% for 1 μm drop. The small droplet (1 μm) also has the largest DF value of -0.0246, behaving in an oblate shape; whereas shape deformation for other size droplets is very limited. The prediction from Taylor's deformation model [42] has deviation up to 83.6 % compared to current simulation. This is because the Taylor model is not suitable for a droplet with varying thermo-physical properties during the melting process.
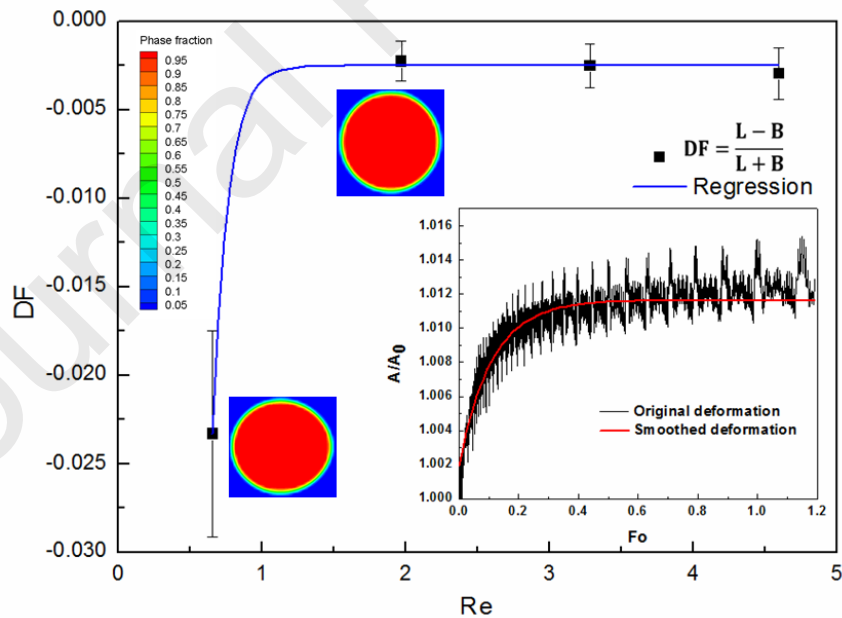

Fig. 6. Deformation rate over Reynolds number for different diameters (1 -7 μm) and same velocity (U=0.66 m/s), scale not proportional. Inset graph shows dimensionless area (A/A_0) over Fo for 3 μm droplet. Two contours represent equilibrium shape of the 1 μm and 3 μm droplet.

To further explore the shape mechanisms for various droplet sizes, the droplet migrations during melting process are monitored and shown in Fig. 7. The dimensionless vertical displacement of the droplet is calculated by dividing the longitudinal position with the height between two plates, depicted against the dimensionless travelling distance, which is the ratio of transverse location and melting length, L_m. The small droplet (1 and 3 μm) tends to stick near the centreline while large ones migrate away from the centreline. The oscillation before equilibrium is expected because surface forces, such as surface tension, changes with the surface temperature and overall thermo-physical properties. Competition between the Buoyance force and thermocapillary force results in the cross-stream migration.
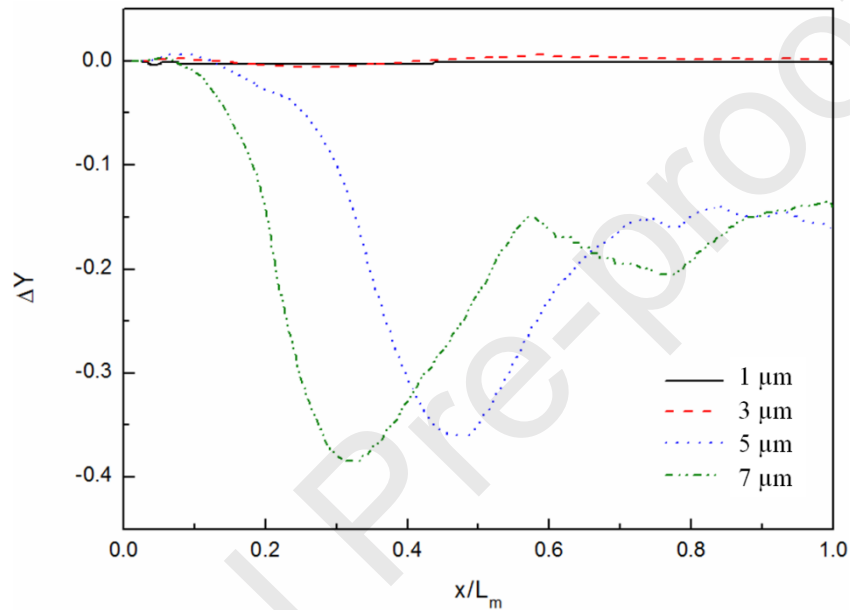

Fig. 7. Dimensionless vertical displacement of droplet centre, ΔY, over the dimensionless melting length, x/L_m, for different droplet sizes (1 -7 μm), U = 0.66 m/s.

In terms of thermocapillary forces, the temperature gradient near the droplet interface induces a surface tension gradient and thereby creates local tangential flows (the Marangoni effect). As a result, several vortices much smaller than the droplet itself appear internally and externally for the droplet, as given in Fig. 8, intensifying the convective heat transfer. Several recirculation following the rear tip of the droplet favour temperature distribution inside and outside the moving PCM droplet. These recirculation patterns, however, could not be captured without the Marangoni effect when surface tension is invariant with temperature [43].

Marangoni effect impacts not only the heat transfer process but also droplet trajectories. It has been experimentally [44] and numerically [45] proved that bubbles or droplets tend to move in a straight path without the Marangoni effect, but move away from the centreline in the presence of Marangoni effect. In the current work, the Marangoni effect of the small

14

droplet is relatively weak because fast uniform temperature is achieved under heat conduction. Hence large oscillation is more obviously for large PCM droplet.
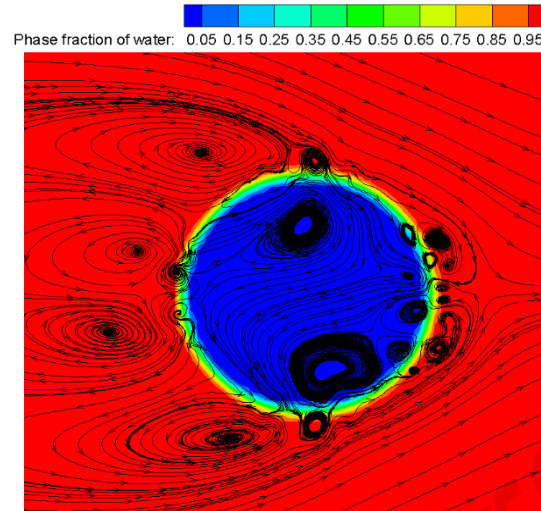

Fig. 8. Streamlines within the droplet at different melting transient Fo = 1.0 under Marangoni effect, D =3 μm and U = 0.66 m/s. Colour indicates the phase fraction of water.

The inset graph of Fig. 9 shows the pressure difference ($\Delta P = P_{max} - P_{min}$) over Fo number in 1 μm droplet (U = 0.66 m/s). At the first instant, the droplet bears the highest pressure due to the sudden acceleration. Then ΔP fluctuates within small local ranges during the melting process and beyond, because of the droplet oscillation nature as aforementioned. To account for the droplet size effect, the equilibrium pressure difference (ΔP_{eq}), by averaging ΔP excluding the highest pressure, is depicted over Re number and given in Fig. 9. For each droplet size, the averaging deviation reaches as high as 17.3%. The smallest emulsion (1 μm) bears the highest pressure, reaching nearly 50000 Pa. With increasing droplet diameter, the equilibrium pressure presents a decreasing exponential trend. The largest pressure gradient acting on the 1 μm interface, as shown in Fig. 9, can easily cause the system instability. It also explains the simulation results by Ma et al. [46], who found the largest pressure drop appears when the particle diameter of MPCM (Micro-encapsulated Phase Change Material) decreases to 1μm.
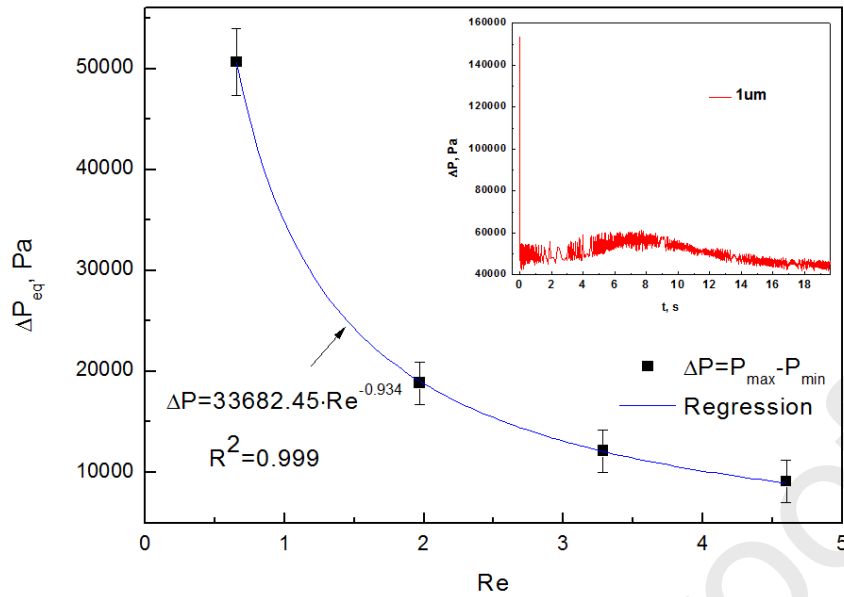
Fig. 9. Equilibrium pressure difference inside PCM droplet over Reynolds number for different diameters (1 -7 μm) and same velocity (U=0.66 m/s). Inset graph present ΔP evolution over melting time in 1 μm droplet.

Fig. 10 illustrates the evolution of the PCM average temperature and surface temperature over melting fraction for different droplet diameters. During the melting process, the average temperature is barely affected by the droplet size, except for the small deviation at the final melting stage (< 5% of the overall temperature increment). In terms of surface temperature, a higher value can be found at a small PCM droplet at the early melting stage ($\beta < 0.5$). At late melting stages, the large droplets (5 μm and 7 μm) favour the growth of surface temperature, resulting in a higher ending surface temperature. The abrupt growth attributes to the cross-stream migration of large droplets given in Fig. 7, which increases velocity components in the longitudinal direction and thus brings chaos velocity inside the droplet, leading to an enhanced overall heat transfer.

The inset graph in Fig. 10 illustrates the melting time over melting fraction. As expected the large droplet requires long melting time. For a given droplet, for example, 7 μm, it takes 0.0002 s to reach melting fraction of 0.5 but requires 0.0008 s to finish the full melting process. The heat conduction driven by a large temperature difference at the beginning of the melting process contributes to the faster melting. With the growing liquid region at the outer layer of the PCM droplet, the smaller temperature difference results in slow melting rate and lower temperature rising for both average and surface temperature. Small temperature differences still exist between the droplet interior and surface area after fully melted, until gradually diminishing and reaching equilibrium temperature over a long travelling distance.
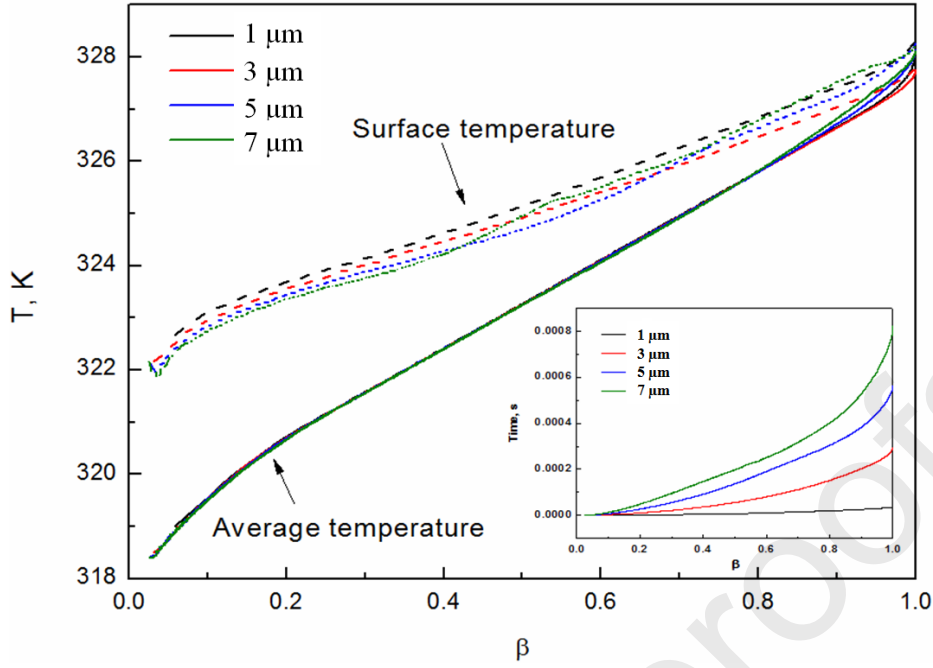
Fig. 10. Evolution of PCM surface and average temperature over melting fraction for different droplet size (1 – 7 μm) and U=0.66 m/s. Inset graph shows the relation of overall melting time and melting fraction.

The Pr number is usually considered to be a constant value for a given bulk PCM [47]. When coming to a single droplet, the description is not accurate enough to present C_p variation during the phase change. Fig. 11 depicts the evolution of Pr number for different droplet sizes against various melting fractions. Under current working conditions, large Pr numbers (>2000) indicates momentum diffusivity dominating the heat transfer behaviour over thermal diffusivity. At the early stage of melting (β < 0.4), Pr number increases almost linearly with melting fraction but is indifferent to the droplet diameters. With the progress of melting, the highest Pr number is spotted for 1 μm and 3 μm droplets, reaching a value of 11544 at β = 0.66. The peak Pr numbers of 5 μm and 7 μm drop are lower than the highest value by 3.77 % and 17.8%, respectively, at a melting fraction around β = 0.62. The presence of peak Pr numbers contributes to the highest C_p value at temperature of 324 K (Fig. 2), which corresponds to the droplet average temperature at melting fraction of 0.65, as given in Fig. 11. Within the large droplet, the temperature distribution is not as homogeneous as the small droplet. This inhomogeneous behaviour leads to differences in averaged viscosity and C_p value, thus leading to different peak Pr number. The increasing droplet temperature compromises the growth of C_p, resulting in a decreasing trend of Pr number at the late melting stage (0.65 < β < 1), until ultimately coming to a value of 2000 when melting ends.
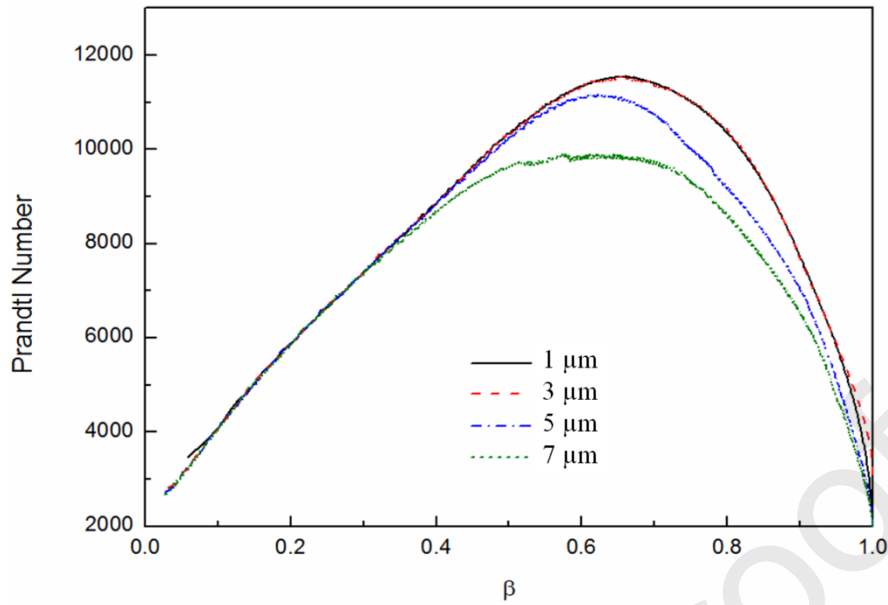
17

Fig. 11. Evolution of Prandtl number of different PCM particle diameters (1 – 7 μm) over the melting fraction.

The energy stored in the PCM droplet during the melting process is examined for different diameters as given in Fig. 12, together with the total energy over the melting fraction given in the inset graph. Unlike the large PCM beads or capsules with diameters of tens of millimetres [26], whose latent heat is several times higher than sensible energy during the melting process, in present work the sensible and latent heat are comparable due to small droplet size. During the melting process, the stored latent heat increases linearly with melting fraction, while the stored sensible energy increases slowly in the early stage of melting and relatively higher in the late stage. The changed trend is determined by the temperature differences between PCM interior and surface as discussed in Fig. 10. For the 1-5 μm droplet, stored sensible heat becomes larger than the latent heat at the late melting stage. For 7 μm droplet, however, latent energy dominates the whole energy storage process because of more participated phase change material. As given in the inset graph, large droplet size favours the total stored energy, and the average total energy of 7 μm is nearly 100 times higher than that of 1 μm.
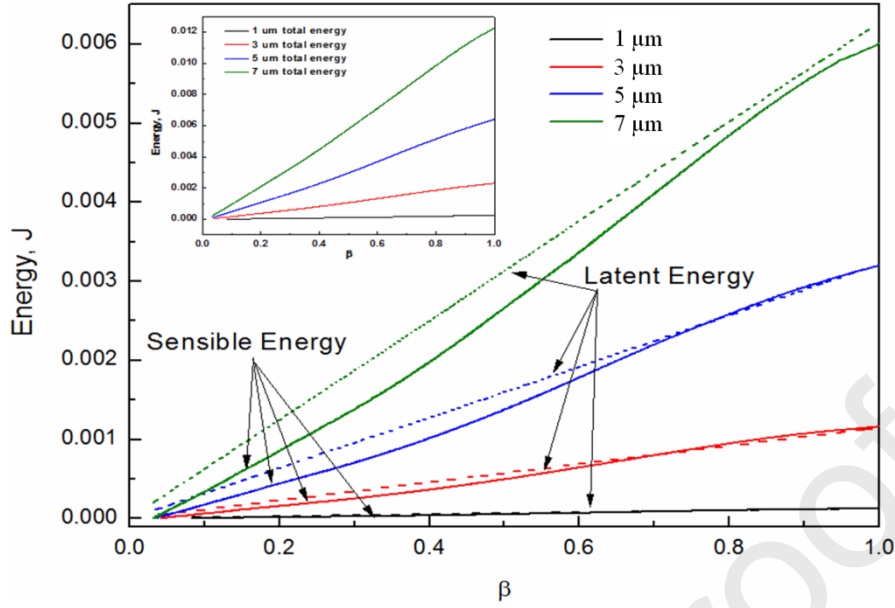
18

Fig. 12. Evolution of stored sensible and latent energy for 3 and 7 μm PCM particle over liquid fraction, U = 0.66 m/s. Inset graph is the total energy (sum of sensible and latent energy) over melting fraction for 1 – 7 μm PCM droplet.

To evaluate the effect of droplet size on the overall heat transfer behaviour, the time and space averaged Nusselt number during melting process is introduced [29], based on heat transfer coefficient in Eq. (11): $\mathrm{Nu_m} = {}^{h_{eff}D}/k_d$. In Fig. 14(a), the evolution averaged Nusselt number ($\mathrm{Nu_m}$) is plotted against Fo number for 1-7 μm droplet under U = 0.66 m/s. It has been found that for all droplet sizes, $\mathrm{Nu_m}$ first decreases from its maximum value to its minimum, then slowly increases to a nearly steady state. The maximum $\mathrm{Nu_m}$ at the first instant is understandable due to high temperature difference. To explain the slight increase trend, the interior averaged velocity inside the droplet is calculated under the same condition and given in Fig. 14(b).

The droplet accelerates under the effect of pressure force and eventually moves in a terminal velocity. It has to be noted that the droplet velocity in Fig. 14(b) is not the terminal velocity due to the short melting time scale. The 1 μm droplet moves at a much lower velocity (~ 0.2 m/s), because the short melting time, which is only 1/8 of that in 7 μm droplet (Fig. 12), does not allow the velocity to develop. A smooth exponential velocity trend is observed for the 3 μm droplet. The acceleration of 5 μm and 7 μm droplets, however, experiences fluctuations due to changing thermo-physical properties. The fluctuation happens at small Fo number (< 0.25), bringing in a sudden velocity increment and enhanced sensible heat. This explains the Nusselt number increase at Fo < 0.25 in Fig. 14(a).

The evolution of Nu number in 1 μm and 3 μm droplets is comparable despite of the large velocity difference. This is because conduction is the main driving reason within the small domain of the 1 μm droplet, while for 3 μm it is the combined effect of conduction and

19

convection. Therefore convection-caused sensible heat is more important in 3 μm, leading to a higher Ste number which is consistent with Ste number variation in Fig. 13. In the inset graph of Fig. 13(a), a simple relationship of total averaged Nusselt number (Nu_{tot}, by averaging Nu_m along the melting evolution) is depicted over Re number. When the droplet size increases from 1 μm to 7 μm, Nu_{tot} number is increased by 2.67 times. The 1 μm PCM droplet, which presents the lowest Nusselt number but highest internal pressure difference, is not beneficial for long-term system operation.
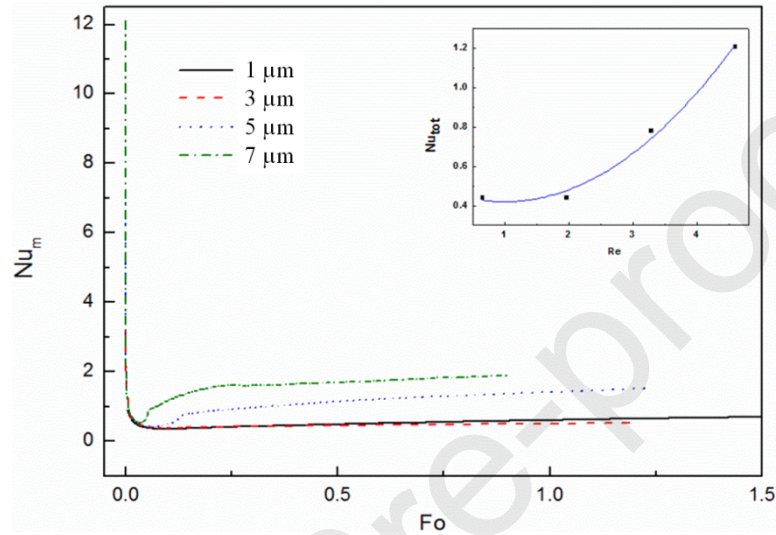
(a)
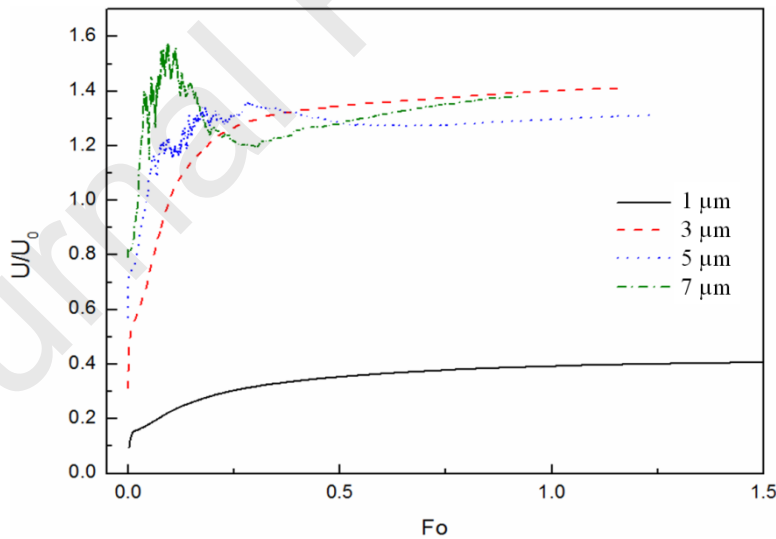
(b)

Fig. 13. (a) Time and space averaged Nusselt number and (b) space averaged dimensionless velocity inside PCM droplet over Fo number for different diameter (1 -7 μm), U=0.66 m/s. Inset graph of (a) shows total averaged Nusselt number over Reynolds number for different size droplets.

3.3. Effect of velocity

In Fig. 14, shape deformation is depicted against Re number, under various inlet velocities for 3 μm PCM emulsion droplet. The DF values are averaged over the melting process, due to the oscillating nature of the small moving droplet, and the deviation falls in the range of 39 %. The negative DF values indicate droplets always perform an oblate shape. The largest deformation is found at the lowest velocity, following an exponential decreasing function with the increment of Re number. When velocities increase 5 times from 0.22 m/s to 1.1 m/s, the absolute DF value decreased nearly 3 times from 0.0091 to 0.0031. Overall the effect of velocity on shape deformation is less significant compared to droplet size.
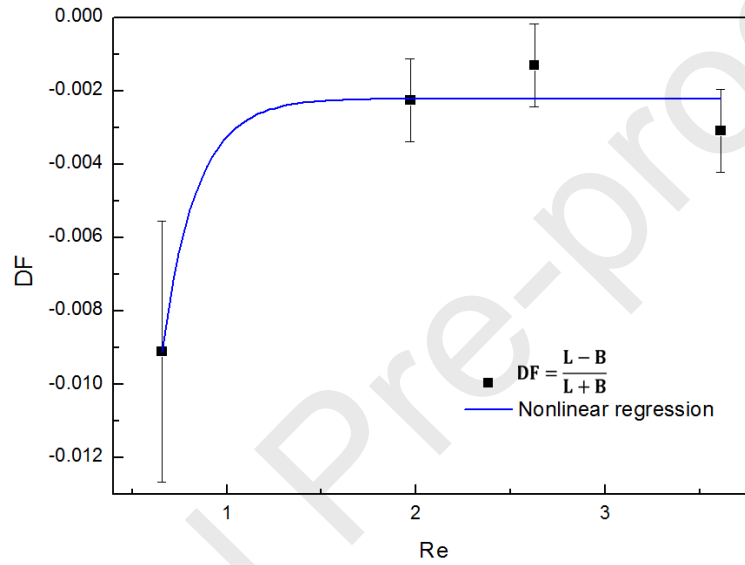
Fig. 14. Deformation rate over Reynolds number under various inlet velocities
$(U = 0.22 - 1.1$ m/s), for $D = 3 \mu$m PCM droplet.

Similarly the effect of velocity on droplet equilibrium pressure difference is found less significant than the droplet size. In Fig. 15, the pressure difference inside the droplet is averaged over melting process due to oscillation features, and depicted over Re number. ΔP_{eq} increases almost linearly with increasing fluid velocity, which is expected because ΔP in either Poiseuille flow [36] or a single droplet increases linearly with U. When U is increased by 5 times, the growth of ΔP is only 25.77%, and its influence is limited if pumping energy is considered in a converter cooling system. The pressure gradient distribution, as given in Fig. 1, concentrates on the droplet boundary where the emulsifier is distributed.

21

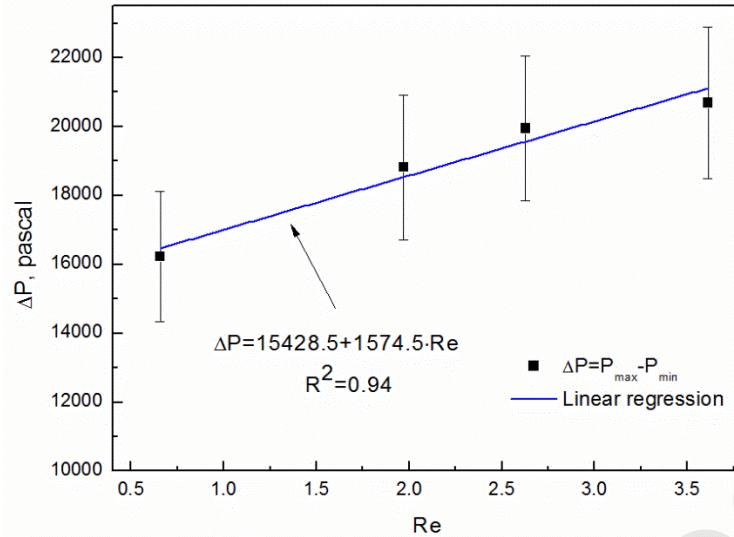Fig. 15. Equilibrium pressure difference inside the droplet over Reynolds number under different velocities (U = 0.22 − 1.1 m/s), for D=3 μm droplet

In Fig. 16, the evolution of stored sensible and latent stored energy inside 3 μm PCM droplet under U=0.22 m/s–1.1 m/s are depicted against Fo time, as well as the total stored energy given in the inset graph. Both the sensible and latent energy show a similar trend with increasing Fo number: increase sharply within short Fo number and reach steady state until melting completion. At the initial heat transfer process (Fo < 0.3), the stored latent energy is always higher than sensible energy, because of the weak convection effect in droplet acceleration process. Faster melting can be observed for high velocity, due to the strong convection and diffusion-control melting effect at late melting stage. An almost equal stored energy is reached at the end of melting because of the same water temperature. Fig. 17 illustrates the relationship between Nu number and Re number under various velocities for 3 μm droplet. The evolution of Nu number under U = 0.22 m/s, as given in the inset graph, shows a decreasing exponential function over Fo number. A linear relationship between the averaged Nu and Re number can be observed. This is because the domain heat transfer mechanism, convection, is enhanced via Marangoni vortices proportional to velocity strength. The Nu number is increased merely 52 % when velocity rising 5 times.
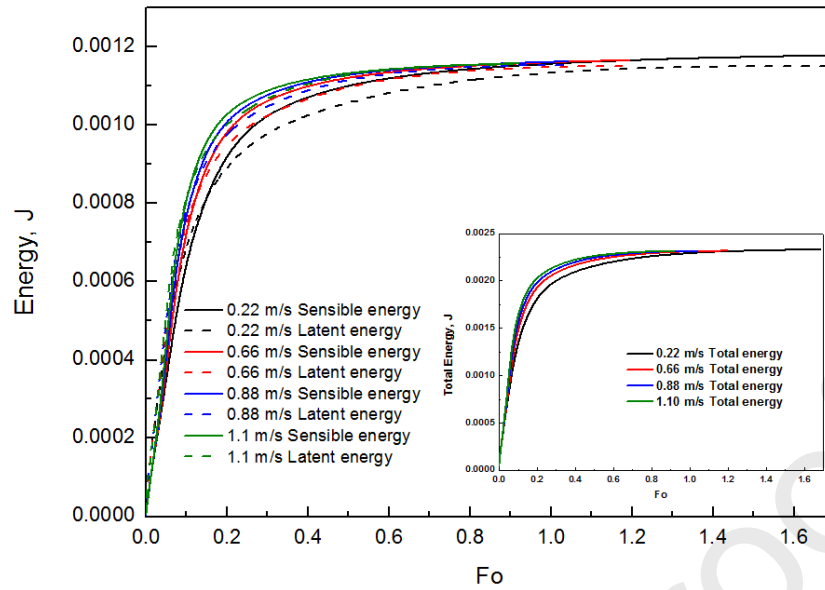
Fig. 16. Evolution of stored sensible and latent energy over Fo number under different velocities (U = 0.22 − 1.1 m/s), for D = 3 μm droplet. Inset graph is the total energy (sum of sensible and latent energy) over Fo number under the same conditions.
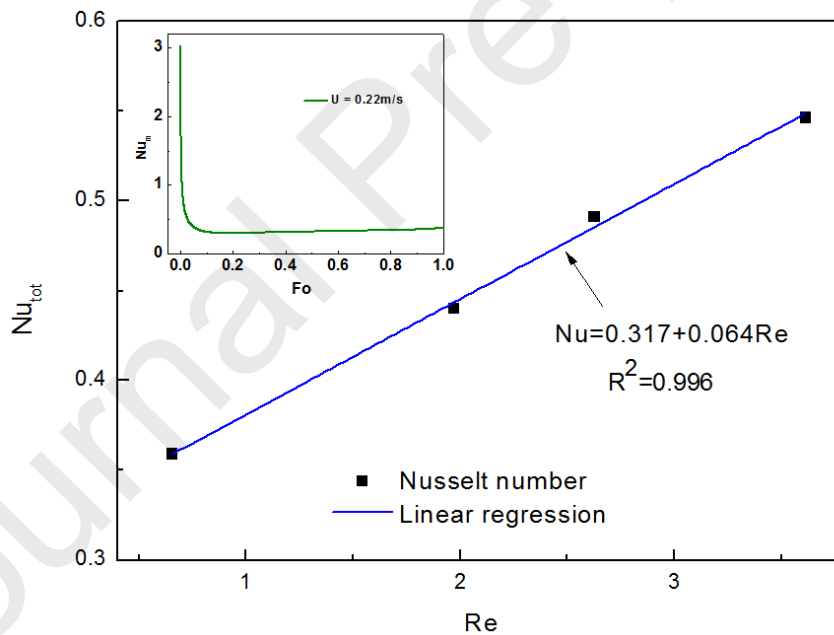
Fig. 17. Averaged Nusselt number inside 3 μm PCM droplet over Reynolds number under different velocities (U = 0.22 − 1.1 m/s). Inset graph shows the Nusselt number evolution over Fo number under U = 0.22 m/s.

23

3.4. Effect of water temperature

The melting process may not complete if inappropriate PCM material is used or temperature field is not fully developed. To study the melting features of this cases, the temperature of continuous water are chosen to be $T_w = 323.325$ K, which allows half of the PCM material to melt. Fig. 18 shows the evolution of stored energy of the 3 and 7 μm droplets under various melting fraction. Within the limited melting range, latent energy dominates heat transfer over sensible heat. The total energy is only half of the fully melted case in Fig. 12.
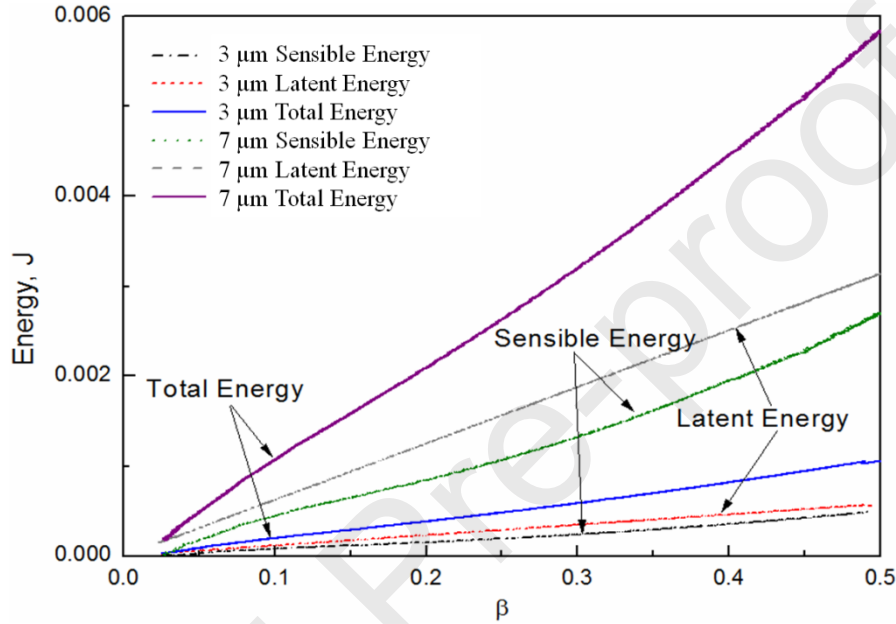
Fig. 18. Evolution of stored sensible, latent and total energy inside 3 μm and 7 μm droplets over various melting fraction, $T_w = 323.325$ K.

In the inset graph of Fig. 19, the time and space averaged Nu number in 1 and 3 μm droplets is depicted over Fo number. It is noteworthy that Nu_m number is calculated over the whole domain, rather than limiting in the melting process as shown in Fig. 14(a), because the half melted condition lasts. At the late heat transfer process, small temperature differences between the droplet surface and surrounding fluid is detected, and it brings rapid growth of Nu_m in 1 μm droplet. The Nu_m evolution of 5 and 7 μm droplet is very similar to 3 μm one thus not depicted. A comparison of total averaged Nu number of fully and half melted cases is depicted over Re number in Fig. 21, for 1-7 μm droplet under $U = 0.66$ m/s. It can be found Nu_{tot} is enhanced 8 times in 1 μm droplet compared to the fully melted condition.

24

Fig. 19. Total averaged Nusselt number inside $1 - 7$ µm PCM droplet over Reynolds number, U = 0.66 m/s. Inset graph shows the Nusselt number evolution over Fo number under half melted condition, T_w = 323.325 K.

3.5. Effect of electric field

Fig. 20 shows the deformation rate over Re number for different diameters (1-7 µm) under U = 0.66 m/s, with and without electrical field. Th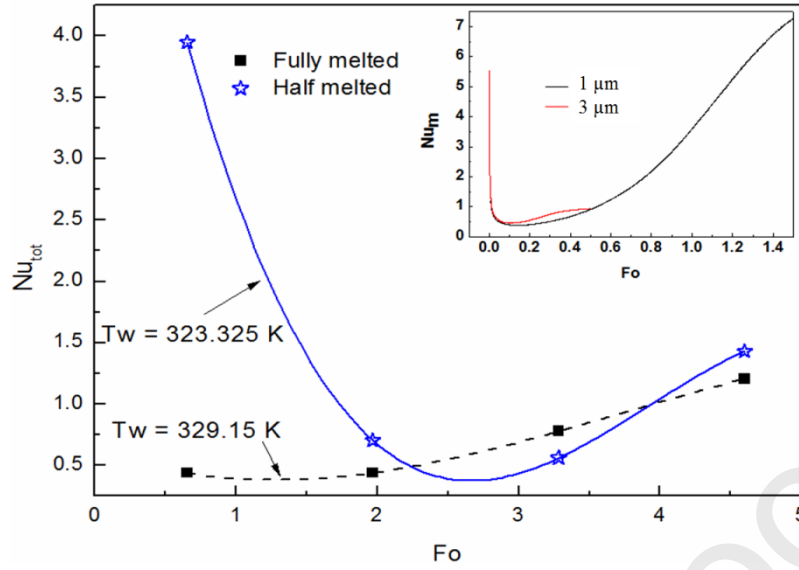e electrical field intensity is chosen to be $E_0 = 25000$ V/m, which falls in operational condition of a HVDC transmission system (provided by GEIRI, Germany). Similar to the no electric case, DF under electrical field has the largest value at 1 µm PCM droplet, and decreases with increasing droplet diameter. In the presence of electricity, the DF value is nearly unchanged for 1 and 3 µm droplets, but become positive for larger diameter, meaning the droplet shape develops from oblate to probate. The development is caused by the additional electric stress. When the PCM droplet and surrounding fluid are exposed to the current electric field, the positive charges accumulate on the upper interface while negative on the bottom. It is noteworthy that the charge distribution is time-dependent due to thermal physical variation during the melting process, but the general layout is unchanged. The electric stress across the droplet interface can therefore be obtained from Eq. (19), and an example of streamwise and cross-stream component distribution across 7 µm drop interface is given in Fig. 21. In the streamwise direction, positive and negative electric stress acts on the left and right side of the droplet, squeezing it to prolate shape. The stress on cross-stream direction is not so distinctive as streamwise direction, but a positive bottom region and negative top region can be identified. A quantitative comparison of the two-direction stresses is given in Fig. 22 following clockwise direction, and the respective starting point (0 degree) is given in Fig. 21. The streamwise

squeeze effect is confirmed as the value on left and right side are almost identical, reaching an average value of 6.6E+06 and -7.1E+06 V/m, respectively. The bottom positive values of the cross-stream stress, however, are much stronger than the top negative values, with average value of 9.1E+06 and -6.8E+06 V/m, respectively. Thus the net electric stress induces lift effect and upward droplet migration. The electric force on small droplet is not strong enough for shape deformation, therefore the shape change only occurs on large drops as given in Fig. 21.
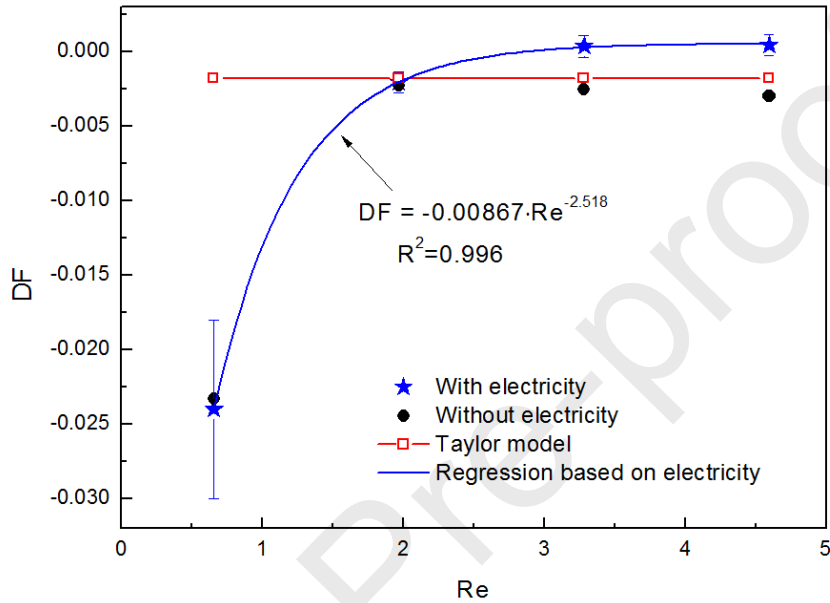
Fig. 20. Deformation rate over Reynolds number for different diameters (1 -7 μm) under electrical field $E_0 = 25000$ V/m, $U = 0.66$ m/s.

To reveal the effect of the background flow field, the steady state DF value predicted from Eq. (19) is also shown in Fig. 20, which is a constant negative value under the current uniform electrical intensity. The DF value of the moving charged droplet, however, does not show a clear combination of the DF from background flow and pure electric effects. Therefore, the EHD feature is not a simple linear combination effects of Poiseuille flow, thermal or electric field, especially under the melting process. A similar conclusion is also given by [24], who only consider the effect of flow field and electric field.
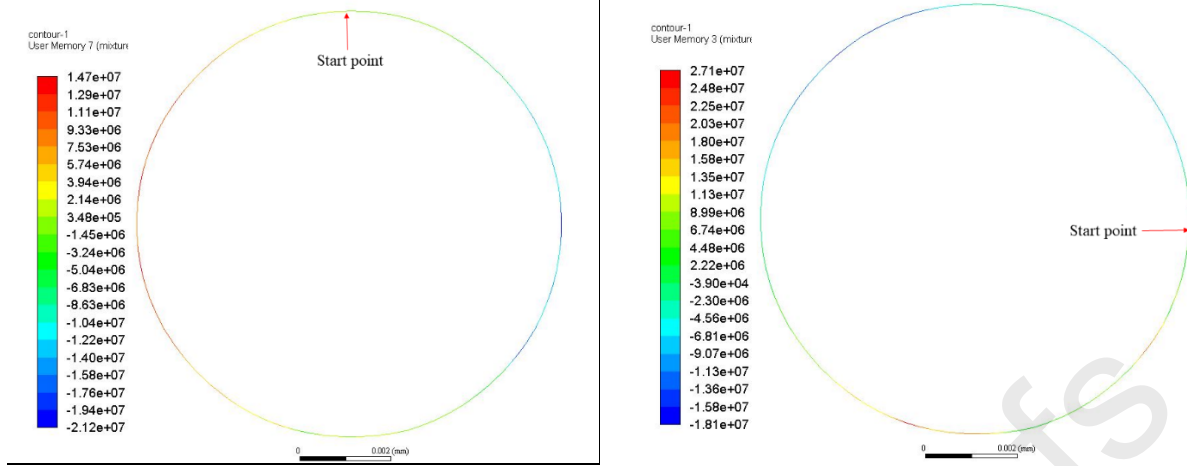
Fig. 21. Electric stress distribution on the droplet interface (iso-surface of C = 0.5) in streamwise (left) and cross-stream (right) direction under E_0 = 25000 V/m, D =7 μm, U = 0.66 m/s.
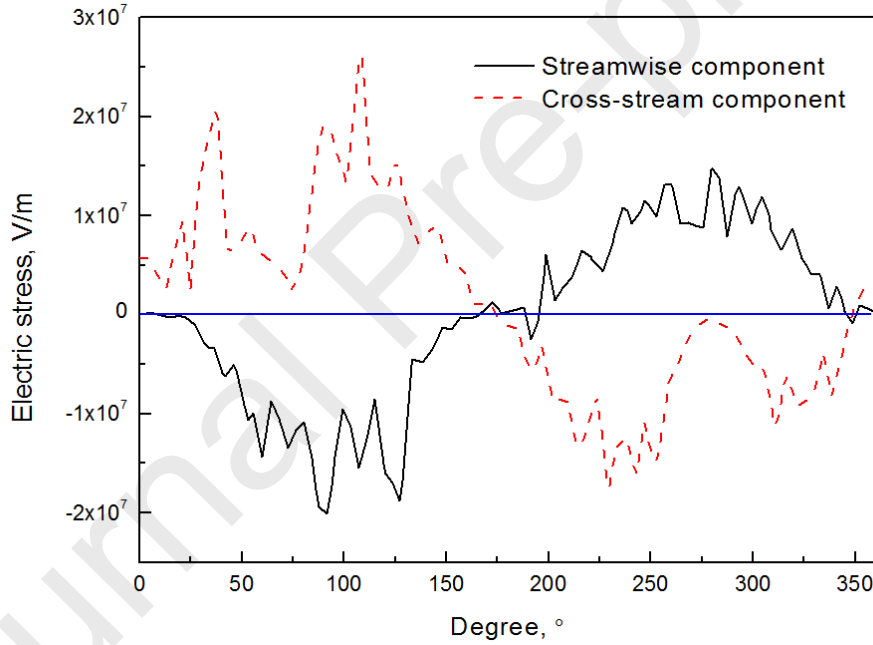
Fig. 22. Electric stress distribution along the droplet Perimeter length from the left tip following an clockwise direction under E_0 = 25000 V/m, D =7 μm, U = 0.66 m/s.

To explore the combined effect of electrical potential and flow field, the droplet migration is monitored with and without electricity field and is depicted in Fig. 23. An equilibrium position is almost achieved when $L_m/D > 100$ for all cases. It is believed no further cross-stream migration will develop considering the small droplet size [48]. The effect of electrical force on large droplet migration is more significant, changing from $\Delta Y = -0.085$ to nearly 0 for 7 μm, caused by the lift electric force in the cross-stream direction. When the electric stress on the charged droplet is balanced over the viscous drag force, the droplet finally

27

moves at a steady speed at an equilibrium position in the viscous fluid. The changes in trajectory of the small droplet under electric effect are almost neglected.

The EHD feature is not a simple linear combination of two distinct effects: Poiseuille flow or electric field. Shape deformation caused by Poiseuille flow alters the electric distribution on the droplet surface, changing electrical stress acting on the PCM droplet. The electrical force influences the flow field inside the outside of the droplet, and ultimately affects the hydrodynamic forces, leading to a renewed shape deformation. Thus the electric potential and flow field are nonlinearly coupled via charge convection and shape deformation.
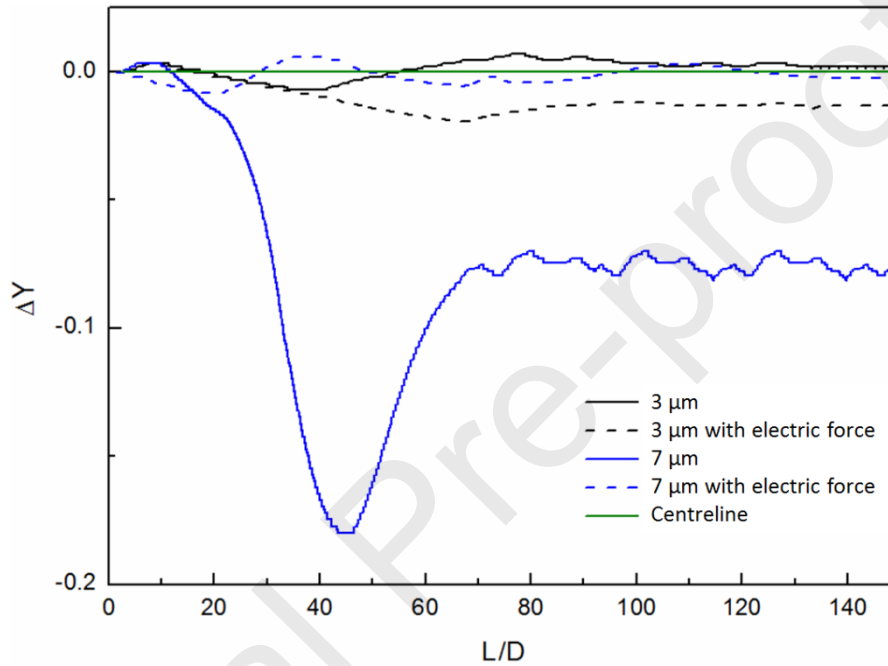
Fig. 23. Dimensionless vertical displacement of the droplet centre, ΔY, over the relative moving length, L/D, for 3 µm and 7 µm droplet size, U = 0.66 m/s, E_0 = 25000 V/m.

The changed net forces and droplet trajectory influences the surrounding flow field and thus speeds up or slows down the melting process. To study the influence of the electrical field on the PCM droplet melting, the total averaged Nu numbers are compared with the value without electricity for different droplet sizes in Fig. 24. The temperature evolution is barely unchanged for the 1 µm and 3 µm droplet. However, as given in the inset graph, temperature is slightly lower in the presence of the electrical field for 5 µm and 7 µm, with deviation up to 2.31% and 5.56 % of ΔT, respectively. Along with the diminish of cross-stream migration, the decreased longitude velocity component weakens heat convection and Marangoni effect, leading to a slower temperature evolution when exposing to electrical field. The changes in temperature reflect in average Nu number, which stays unchanged for 1 and 3 µm droplet but decreases by 16.94 % and 53.90 % for 5 and 7 µm, respectively. Nevertheless, the increasing exponential function with the growth of the droplet size remains. A comparison of pressure difference with and without the effect of electric field is given in Table. 1. The pressure

difference for both cases decreases with increasing droplet size, with a slight reduce of average deviation of 5.74% for electrical case, which is caused by the deformed shape and changed trajectory.
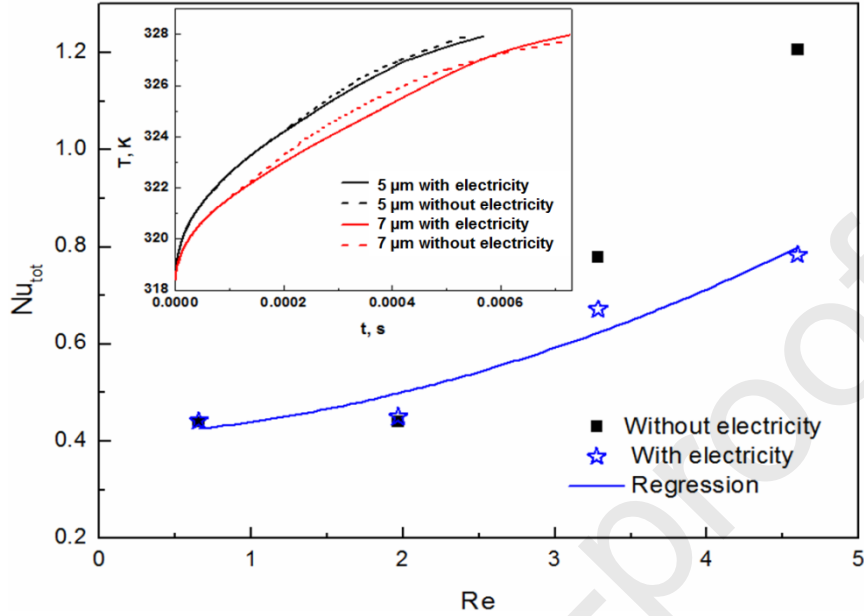
Fig. 24. Comparison of Nusselt number inside various diameters of PCM droplet (1, 3, 5 and 7 μm) without and with electrical field, $E_0 = 25000$ V/m, U = 0.66 m/s. Inset graph is the temperature evolution of 5 μm and 7 μm PCM droplets.

Table 1. Equilibrium pressure difference inside droplet with and without electricity.

Diameter (μm)	1	3	5	7
ΔP_{eq} without electricity (Pa)	50652.79	18844.31	12136.74	9103.75
ΔP_{eq} with electricity (Pa)	49952.52	17401.16	11240.83	8508.68

4. Conclusion

A numerical model was established to describe the shape stability and thermodynamic behaviour of a fatty acid-based PCM slurry for HVDC converter cooling. The simulation included the shear stress from fluid field, thermophysical expansion from thermal field and electrical polarization from electrical field using temperature-dependence properties. The main consequence of electrical field was the electrical polarization stress may deform the PCM droplet, and the electricity-driven flow changed energy evolution inside droplet. When emulsion exposed to high shear rate simultaneously, the PCM may burst the emulsifier shields and ultimately results in complete breakdown of the fluid system. The effects of

droplet size, fluid velocity and temperature, and electrical field were examined. The main conclusions are:

1. The droplet size was the major influencing factor to shape stability under studied operational condition. It was found the 1 μm drop has the largest deformation, with averaged deformation ratio 8 times higher than the 7 μm droplet. The impact of velocity on shape deformation was proved to be much less than the droplet size. The electric stress across surface tended to squeeze the droplet into prolate shape for larger particles, which offset the shape deformation caused by shear stress and stabilized the slurry system.

2. A large pressure gradient was found at the droplet interface, thus special attention should be paid to the elasticity and adhesiveness between PCM core and emulsifier surface. The 1 μm PCM droplet bore the highest interior pressure differences, which was almost 5 times than the large 7 μm drop (0.01 MPa). The growth of slurry velocity only slightly increased the particle interior pressure, about 25.77% when velocity increasing from 0.22 m/s to 1.1 m/s. Due to the squeeze impact of electrical field, the PCM droplet interior pressure was decreased by 5.74 % on average, which showed the stabilization effect caused by electrical field.

3. The latent and sensible energy contributed almost equally to the total energy storage capacity for studied micro- drops. The Nusselt number of small droplet was the lowest, meaning a less efficient energy exchange. This is because conduction dominated the small drops, while convection and vortices inside and outside the large droplet improved heat transfer. The energy exchange is vulnerable to surrounding temperature field, and it can be further enhanced by high working velocity. The introduction of electric field decreased the Nu number of 7 μm drop by 53.9%, due to a different interior and exterior fluid and thermal field of droplet. This means the electric field delaying the energy exchange of micro- droplet, and the effect may be more profound for millimetre scale droplet.

Acknowledgements

Nomenclature

B	length of perpendicular axis of deformed droplet, (m)
C_a	Capillary number
C_o	Courant number
c_p	specific heat capacity, (kJ/kg·K)
D	droplet diameter, (m)
$\vec{E}$	electric field, (V/m)
$\overrightarrow{F_E}$	interfacial tension force
$\overrightarrow{F_S}$	electric body force
Fo	Fourier number
h	heat transfer coefficient, (W/m^2·K)
H	distance, (m)
H_{tot}	total domain width, (m)
k	thermal conductivity, (W/m·K)
L	length of parallel axis of deformed droplet, (m)
L_m	latent heat, (kJ/kg)
L_{tot}	total domain length, (m)
$\vec{n}$	unit normal to the interface
Nu	Nusselt number
P	permittivity ratio
p	pressure, (Pa)
Pr	Prandtl number
r	radial coordinate
Re	Reynolds number
R_0	initial droplet radius, (m)
Ste	Stefan number
t	time, (s)
Δt	time step
T	temperature, (°C)
T_a	average phase-change temperature, (°C)
T_s	Droplet surface temperature, (°C)
$\vec{u}$	velocity vector, (m/s)
U	average velocity, (m/s)

We	Weber number
x	fraction of the surface initially covered by surfactant
Δx	grid size
z	spatial location normal to the interface

Greek symbols

α	thermal diffusivity, (m^2/s)
β	liquid fraction
Γ	surfactant concentration
δ_Γ	dirac delta function
ε	fluid permittivity, (F/m)
η	fluid conductivity, (S/m)
κ	local interface curvature
λ	ratio of the droplet viscosity to the solvent viscosity
μ	viscosity, (kg/(m·s))
ρ	density, (kg/m^3)
σ	surface tension, (N/m)
φ	angular coordinate
Φ	dissipate term

Subscripts

c	continuous phase
CSF	continuum surface force
d	dispersed phase
DF	droplet deformation
eff	effective value
EHD	electrohydrodynamics
HVDC	high voltage direct current
IGBT	insulated gate bipolar transistor
l	liquid phase
L	latent heat
PCM	phase change material

s	solid phase
S	sensible heat
tot	total
VOF	volume of fluid

References

[1]	Giampieri A, Ma Z, Ling Chin J, Smallbone A, Lyons P, Khan I, et al. Techno-economic analysis of the thermal energy saving options for high-voltage direct current interconnectors. Applied Energy. 2019;247:60-77.

[2]	Gomis-Bellmunt O, Junyent-Ferré A, Sumper A, Galceran-Arellano S. Maximum generation power evaluation of variable frequency offshore wind farms when connected to a single power converter. Applied Energy. 2010;87:3103-9.

[3]	Kabalyk Y. Determination of Energy Loss in Power Voltage Inverters for Power Supply of Locomotive Traction Motors. Procedia Engineering. 2016;165:1437-43.

[4]	Lips HP. Technology trends for HVDC thyristor valves. POWERCON '98 1998 International Conference on Power System Technology Proceedings (Cat No98EX151)1998. p. 451-5 vol.1.

[5]	Kandlikar SG, Hayner CN. Liquid Cooled Cold Plates for Industrial High-Power Electronic Devices—Thermal Design and Manufacturing Considerations. Heat Transfer Engineering. 2009;30:918-30.

[6]	Sarı A, Alkan C, Altıntaş A. Preparation, characterization and latent heat thermal energy storage properties of micro-nanoencapsulated fatty acids by polystyrene shell. Applied Thermal Engineering. 2014;73:1160-8.

[7]	Li M, Kao H, Wu Z, Tan J. Study on preparation and thermal property of binary fatty acid and the binary fatty acids/diatomite composite phase change materials. Applied Energy. 2011;88:1606-12.

[8]	Zhang J-J, Zhang J-L, He S-M, Wu K-Z, Liu X-D. Thermal studies on the solid–liquid phase transition in binary systems of fatty acids. Thermochimica Acta. 2001;369:157-60.

[9]	Sarı A, Kaygusuz K. Some fatty acids used for latent heat storage: thermal stability and corrosion of metals with respect to thermal cycling. Renewable Energy. 2003;28:939-48.

[10] Noël JA, Kahwaji S, Desgrosseilliers L, Groulx D, White MA. Chapter 13 - Phase Change Materials. In: Letcher TM, editor. Storing Energy. Oxford: Elsevier; 2016. p. 249-72.

[11] Hasan A, Hejase H, Abdelbaqi S, Assi A, Hamdan M. Comparative effectiveness of different phase change materials to improve cooling performance of heat sinks for electronic devices. Applied Sciences. 2016;6:226.

[12] Corach J, Sorichetti PA, Romano SD. Electrical properties of mixtures of fatty acid methyl esters from different vegetable oils. International Journal of Hydrogen Energy. 2012;37:14735-9.

[13] Kahwaji S, Johnson MB, Kheirabadi AC, Groulx D, White MA. Fatty acids and related phase change materials for reliable thermal energy storage at moderate temperatures. Solar Energy Materials and Solar Cells. 2017;167:109-20.

[14] Shao J, Darkwa J, Kokogiannakis G. Review of phase change emulsions (PCMEs) and their applications in HVAC systems. Energy and Buildings. 2015;94:200-17.

[15] Schramm LL. Fundamentals and applications in the petroleum Industry. Adv Chem. 1992;231:3-24.

[16] Dong Q, Sau A. Electrohydrodynamic interaction, deformation, and coalescence of suspended drop pairs at varied angle of incidence. Physical Review Fluids. 2018;3:073701.

[17] Ouriemi M, Vlahovska Petia M. Electrohydrodynamics of particle-covered drops. Journal of Fluid Mechanics. 2014;751:106-20.

[18] Mikkelsen A, Rozynek Z, Khobaib K, Dommersnes P, Fossum JO. Transient deformation dynamics of particle laden droplets in electric field. Colloids and Surfaces A: Physicochemical and Engineering Aspects. 2017;532:252-6.

[19] Ferrouillat S, Bontemps A, Poncelet O, Soriano O, Gruss J-A. Influence of nanoparticle shape factor on convective heat transfer and energetic performance of water-based SiO2 and ZnO nanofluids. Applied Thermal Engineering. 2013;51:839-51.

[20] Timofeeva EV, Routbort JL, Singh D. Particle shape effects on thermophysical properties of alumina nanofluids. Journal of Applied Physics. 2009;106:014304.

[21] Das Siddhartha, Chakraborty Suman, Mitra Sushanta K. Redefining electrical double layer thickness in narrow confinements: Effect of solvent polarization. Physical Review E. 2012;85:051508.

[22] Das Siddhartha and Chakraborty Suman. Transverse electrodes for improved DNA hybridization in microchannels. AIChE. 2007;53:1086-1099

[23] Das Siddhartha, Das Tamal, Chakraborty Suman. Analytical solutions for the rate of DNA hybridization in a microchannel in the presence of pressure-driven and electroosmotic flows. Sensors and Actuators B. 2006;114:957-963.

[24] Mandal S, Bandopadhyay A, Chakraborty S. The effect of uniform electric field on the cross-stream migration of a drop in plane Poiseuille flow. Journal of Fluid Mechanics. 2016;809:726-74.

[25] Das S, Mandal S, Chakraborty S. Effect of temperature gradient on the cross-stream migration of a surfactant-laden droplet in Poiseuille flow. Journal of Fluid Mechanics. 2017;835:170-216.

[26] Yu Q, Romagnoli A, Al-Duri B, Xie D, Ding Y, Li Y. Heat storage performance analysis and parameter design for encapsulated phase change materials. Energy Conversion and Management. 2018;157:619-30.

[27] Zhao W, Neti S, Oztekin A. Heat transfer analysis of encapsulated phase change materials. Applied Thermal Engineering. 2013;50:143-51.

[28] Ioannou N, Liu H, Zhang YH. Droplet dynamics in confinement. Journal of Computational Science. 2016;17:463-74.

[29] Hase M, Weigand B. Transient heat transfer of deforming droplets at high Reynolds numbers. International Journal of Numerical Methods for Heat & Fluid Flow. 2004;14:85-97.

[30] Brackbill JU, Kothe DB, Zemach C. A continuum method for modeling surface tension. Journal of computational physics. 1992;100:335-54.

[31] Wang Z, Dong Q, Zhang Y, Wang J, Wen J. Numerical Study on Deformation and Interior Flow of a Droplet Suspended in Viscous Liquid under Steady Electric Fields. Advances in Mechanical Engineering. 2014;6:532797.

[32] Hua J, Lim LK, Wang C-H. Numerical simulation of deformation/motion of a drop suspended in viscous liquids under influence of steady electric fields. Physics of Fluids. 2008;20:113302.

[33] Zuo Z, Wang J, Huo Y, Fan Y. Numerical study of droplet evaporation in coupled high-temperature and electrostatic fields. Advances in Mechanical Engineering. 2015;7:1-11.

[34] Taylor GI, McEwan AD, Jong LNJd. Studies in electrohydrodynamics. I. The circulation produced in a drop by an electric field. Proceedings of the Royal Society of London Series A Mathematical and Physical Sciences. 1966;291:159-66.

[35] Talimi V, Muzychka YS, Kocabiyik S. A review on numerical studies of slug flow hydrodynamics and heat transfer in microtubes and microchannels. International Journal of Multiphase Flow. 2012;39:88-104.

[36] Li Q, Angeli P. Experimental and numerical hydrodynamic studies of ionic liquid-aqueous plug flow in small channels. Chemical Engineering Journal. 2017;328:717-36.

[37] Kékesi T, Amberg G, Prahl Wittberg L. Drop deformation and breakup. International Journal of Multiphase Flow. 2014;66:1-10.

[38] Kékesi T, Amberg G, Prahl Wittberg L. Drop deformation and breakup in flows with shear. Chemical Engineering Science. 2016;140:319-29.

[39] Torza S, Cox RG, Mason SG, Taylor GI. Electrohydrodynamic deformation and bursts of liquid drops. Philosophical Transactions of the Royal Society of London Series A, Mathematical and Physical Sciences. 1971;269:295-319.

[40] Nadim A, Stone HA. The Motion of Small Particles and Droplets in Quadratic Flows. Studies in Applied Mathematics. 1991;85:53-73.

[41] Smolianski A, Haario H, Luukka P. Numerical study of dynamics of single bubbles and bubble swarms. Applied Mathematical Modelling. 2008;32:641-59.

[42] Taylor GI. The formation of emulsions in definable fields of flow. Proceedings of the Royal Society of London Series A, Containing Papers of a Mathematical and Physical Character. 1934;146:501-23.

[43] Wang J, Yang C, Mao Z. Numerical simulation of Marangoni effects of single drops induced by interphase mass transfer in liquid-liquid extraction systems by the level set method. Science in China Series B: Chemistry. 2008;51:684-94.

[44] Wegener M, Grünig J, Stüber J, Paschedag AR, Kraume M. Transient rise velocity and mass transfer of a single drop with interfacial instabilities – experimental investigations. Chemical Engineering Science. 2007;62:2967-78.

[45] Engberg RF, Wegener M, Kenig EY. The impact of Marangoni convection on fluid dynamics and mass transfer at deformable single rising droplets – A numerical study. Chemical Engineering Science. 2014;116:208-22.

[46] Ma F, Zhang P, Shi XJ. Investigation of thermo-fluidic performance of phase change material slurry and energy transport characteristics. Applied Energy. 2018;227:643-54.

[47] Wang X, Niu J, Li Y, Zhang Y, Wang X, Chen B, et al. Heat transfer of microencapsulated PCM slurry flow in a circular tube. AIChE Journal. 2008;54:1110-20.

[48] Wegener M, Fevre M, Paschedag AR, Kraume M. Impact of Marangoni instabilities on the fluid dynamic behaviour of organic droplets. International Journal of Heat and Mass Transfer. 2009;52:2543-51.

Highlights:

- Shape stability of PCM slurry studied in fluid-thermo-electric coupled field
- Effects of electric field, particle size, and fluid conditions studied
- Electric field favours slurry stability but slows down energy charging rate
- Enhanced convection caused vortices near droplet improves heat transfer

Dear Editor-in-Chief,

We would like to submit the enclosed manuscript entitled "Shape stability and thermodynamic study of phase change material slurry under fluid-thermo-electric coupled fields for electronic device cooling", which we wish to be considered for publication in Applied Thermal Engineering. We declare that we do not have any commercial or associate interest that represents a conflict of interest in connection with the work submitted.

If you have any queries, please do not hesitate to contact me at the address below.

Thank you very much for your time and consideration.

Kind Regards,

Yours sincerely,

Qi Li & Chuan Li & Yulong Ding

School of Chemical Engineering

University of Birmingham

Birmingham, B15 2TT, United Kingdom

Email: q.li.2@bham.ac.uk; / c.li.4@bham.ac.uk